Diamond optomechanical cavity with a color center for coherent microwave-to-optical quantum interfaces

Byunggi Kim,[1,*] Hodaka Kurokawa,[2] Katsuta Sakai,[3,4] Kazuki Koshino,[2,3] Hideo Kosaka,[2,5] and Masahiro Nomura[1,†]

[1] *Institute of Industrial Science, The University of Tokyo, 4-6-1 Komaba, Meguro, Tokyo 153-8505, Japan*

[2] *Quantum Information Research Center, Institute of Advanced Sciences, Yokohama National University, 79-5 Tokiwadai, Hodogaya, Yokohama 240-8501, Japan*

[3] *College of Liberal Arts and Sciences, Tokyo Medical and Dental University, 2-8-30 Konodai, Ichikawa, Chiba 272-0827, Japan*

[4] *KEK Theory Center, Institute of Particle and Nuclear Studies, High Energy Accelerator Research Organization, 1-1 Oho, Tsukuba, Ibaraki 305-0801, Japan*

[5] *Department of Physics, Graduate School of Engineering Science, Yokohama National University, 79-5 Tokiwadai, Hodogaya, Yokohama 240-8501, Japan*

(Received 21 May 2023; revised 5 September 2023; accepted 26 September 2023; published 13 October 2023)

Quantum transduction between microwave and optical photons plays a key role in quantum communication among remote qubits. Although the quantum transduction schemes generating communication photons have been successfully demonstrated by using optomechanical interfaces, the low conversion efficiency remains an obstacle to the implementation of a quantum network consisting of multiple qubits. Here, we present an efficient quantum transduction scheme using a one-dimensional diamond optomechanical crystal cavity tuned at a color-center emission without optomechanical coupling. The optomechanical crystal cavity incorporates a thin aluminum nitride (AlN) pad piezoelectric coupler near the concentrator cavity region, while retaining ultrasmall mechanical and optical mode volumes of about $1.5 \times 10^{-4}(\Lambda_p)^3$ and $0.2(\lambda/n)^3$, respectively. The energy level of a coherent color-center electron is manipulated by a strong mechanical-mode–color-center electron-coupling rate up to 16.4 MHz. In our system, we theoretically predict that the population-conversion efficiency from a single microwave photon into an optical photon can reach 15% combined with current technologies. The coherent conversion efficiency is over 10% with a reasonably pure decay time of $T_2^* > 10$ ns. Our results imply that an atomic color center strongly coupled to the optomechanical crystal cavity will offer a highly efficient quantum transduction platform.

DOI: 10.1103/PhysRevApplied.20.044037

I. INTRODUCTION

Quantum transduction platforms for a single microwave-to-optical conversion are of paramount interest for quantum networks between microwave-controlled qubits. For this purpose, the use of the optomechanical interface [1–6] has emerged as an efficient way to convert between microwave and optical photons. The scheme using a one-dimensional (1D) optomechanical cavity typically integrates a piezoelectric coupler and phononic waveguide [1,2,7]. A microwave photon produces a phonon with the same frequency as that required to couple with an optical photon in optomechanical interfaces via photoelastic and moving-boundary effects [8–10]. The cavity-enhanced interaction between photon and phonon exerts frequency modulation of an optical photon, thereby enabling quantum transduction.

In the last decade, a quantum interface using a diamond color center has attracted enormous attention for the generation of remote entanglement between coherent spin qubits [11–14]. The photonic nanocavity with high cooperativity enables control of the spin and orbital states of the color-center electron [15,16], leading to the large-scale integration of multinode quantum processors [17]. In addition, spin memory-enhanced quantum interfaces have been implemented via the optomechanical system [18]. However, the low microwave-to-optical conversion efficiency remains a challenge for the implementation of the multinode quantum network. The optomechanical interface requires significant photonic cooperativity of the optomechanical cavity with a large number of pumping photons [19,20], which generates critical thermal noise in the subkelvin temperatures. To suppress thermal noise, we proposed quantum interfaces using diamond spin memory

*bkim@iis.u-tokyo.ac.jp
†nomura@iis.u-tokyo.ac.jp

with photonic cavity-enhanced emission [21]. Our theoretical predictions suggested that the optical pump power decreased by 2–3 orders of magnitude while maintaining an entanglement-generation rate of several tens of kilohertz.

Here, we investigated the feasible design of a quantum transduction system enabling microwave-to-optical conversion via a strong mechanical-mode–color-center electron interaction inside the diamond optomechanical crystal cavity. Specifically, the piezoelectric aluminum nitride (AlN) thin-film pad on the 1D nanobeam optomechanical crystal is used to couple with microwave-emitting qubits, while keeping the ultrasmall mode volume of the mechanical and optical modes. The mechanical-mode–color-center interaction enables manipulation of the coherent electron-energy level in a charged nitrogen-vacancy center (N-V^-) in diamond, followed by emission of an optical photon without optomechanical coupling. Furthermore, we discuss the performances of the microwave-to-optical conversion by providing the time evolution of the quantum population. The simulation results indicate that a color-center electron emits a photon to the optical waveguide with a microwave-to-optical conversion efficiency of 15%. Furthermore, we calculated the microwave-to-optical coherent conversion efficiency to be as high as 10% with a pure dephasing time of the N-V^- of $T_2^* = 10$ ns. Hence, we expect that our scheme can be applied to efficient quantum networks with embedded coherent spin memories.

II. RESULTS AND DISCUSSION

A. Quantum interface between a superconducting qubit and an optical photon

Figure 1(a) shows a schematic of the quantum transduction scheme between a superconducting qubit and a cavity photon. Our quantum interfaces include three cavities of microwave photon, phonon, and optical photon. The microwave resonator contains a piezoelectric transducer of a thin-film AlN pad to convert the microwave photon into a phonon, which is excited by the noncontact electrode pair. The generated cavity phonon tunes the energy level of the electron via the interaction between the mechanical mode and the color-center electron. In this study, we consider the use of the N-V^-, of which the zero-phonon line, ω_{ZPL}, is resonant at 470 THz. Use of the N-V^- center benefits from facile manipulation of the energy level at the excited state [22]. As shown in Fig. 1(b), the optical photon excites the energy level of the electron at the photonic cavity, with an external optical driving frequency of ω_d. The mechanical-mode–color-center interaction changes the energy level of the electron by $\hbar\omega_m$, such that $\omega_{\mathrm{ZPL}} = \omega_d + \omega_m$. Here, the frequency of the photonic cavity, ω_{opt}, includes both optical driving, ω_d, and modulated frequencies, $\omega_d + \omega_m$, to satisfy linewidth-limited modulation conditions:

$$\omega_{\mathrm{opt}} - \gamma_{\mathrm{opt}}/2 < \omega_d < \omega_{\mathrm{opt}} + \gamma_{\mathrm{opt}}/2, \tag{1.1}$$

$$\omega_{\mathrm{opt}} - \gamma_{\mathrm{opt}}/2 < \omega_d + \omega_m < \omega_{\mathrm{opt}} + \gamma_{\mathrm{opt}}/2, \tag{1.2}$$

where γ_{opt} is the linewidth (decay rate) of the photonic cavity. Thus, the state of the superconducting qubit can be transferred to the cavity photon thorough the optical waveguide.

B. Design of the optomechanical cavity

Figure 2(a) shows the design of the 1D nanobeam system accommodating the microwave resonator and the optomechanical cavity. The optomechanical cavity consists of photonic and phononic mirror cells and eight cavity cells. The AlN pad is placed on top of the mirror region to convert a microwave photon into a phonon via piezoelectric coupling. Mechanical mode matching should be realized for efficient coupling between the microwave resonator and optomechanical cavity. In addition, mechanical waveguide loss can be reduced by optimizing the distance between a piezoelectric material and the cavity region of the optomechanical crystal. From these points of view, we considered the use of the small AlN pad near the cavity as a piezoelectric resonator.

Cavities with ultrasmall mode volumes have been extensively investigated for rapid manipulation of electron orbits [23–27]. Specifically, the use of concentrators at the cavity is a simple and robust approach to achieve ultrasmall mode volumes for both photonic [27–30] and phononic modes [23,26]. The inset of Fig. 2(a) describes the detailed design of the concentrators. In our cavity design, the radius of curvature at the concentrator tip was set at 30 nm, considering a typical fabrication resolution by electron beam lithography. Figure 2(b) shows the geometry of the unit cells of the optomechanical cavity. Geometries of the outer half-ellipse are indicated for the central cavity holes. We performed a finite-element-method (FEM) simulation to design the optomechanical cavity. The cavity-resonant frequencies are $\omega_{\mathrm{opt}} \sim 470$ THz and $\omega_m \sim 12.5$ GHz for the photon and phonon, respectively.

The asymmetric design of the mirror allows phononic quasiwaveguiding from the left side and photonic quasiwaveguiding from the right side. Figures 2(c)–2(f) show the photonic and phononic band structures of the left and right sides of the beams. As shaded in Fig. 2(b), the band gaps are filled by purple and red for the left and right sides, respectively. For the mechanical vibration, the band gaps of the breathing modes are indicated with the adjacent breathing modes as black bold lines. The vibrational modes inside the breathing band gaps are orthogonal to the breathing mode due to differences in symmetry so that no interference occurs. We optimized the unit-cell geometries to implement partial mirrors by adjusting the position

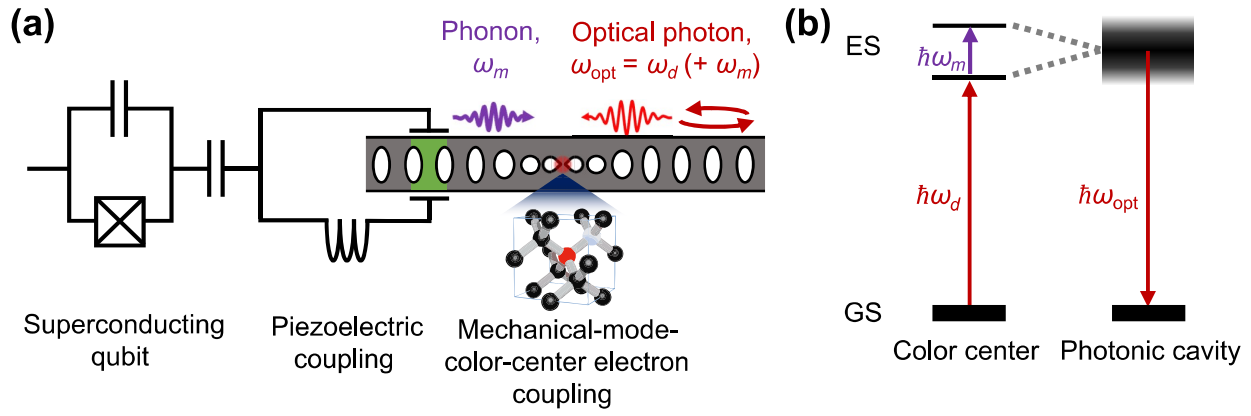

FIG. 1. Schematic illustration of the microwave-to-optical conversion scheme via a diamond color-center spin memory. (a) Quantum interfaces to convert a microwave photon generated by a superconducting qubit to the photon tuned at the color-center emission. (b) Energy level of the color-center electron included in that of the photonic cavity.

of the resonant frequencies within the band gaps. For the left (right) side of the beam, the photonic (phononic) resonant frequency was set in the range of ±15 THz (±1.5 GHz) from the band-gap center to prevent energy leakage. On the other hand, the phononic (photonic) resonant frequency was shifted 1.5 GHz (15 THz) away from the band edge, enabling external input and output. Coupling to the external optical waveguide was realized by changing the number and period of photonic partial mirror cells while maintaining the mechanical quality factor. The cavity and the unit-cell period with the AlN pad were optimized to maximize the optical quality factor using the Nelder-Mead method, which is accepted as one of the efficient ways to design of a 1D optomechanical cavity with several geometrical parameters [7,31,32]. The period of the mirror cell with the AlN transducer was optimized to $a - 20.6$ nm to maximize the optical quality factor.

Figures 2(g)–2(i) show the FEM simulation results of the mechanical resonant mode, the electric potential field profile under the mechanical resonance, and the optical resonant mode, respectively. The optical mode profile in Fig. 2(i) was calculated in the presence of Al to take into account scattering of the evanescent fields. To maximize piezoelectric coupling, we considered the deposition of *m*-plane AlN on the diamond slab. Although the growth of the *m*-plane AlN thin film is technologically difficult, remarkable experimental works have been reported by using metal-organic chemical vapor deposition [33] and plasma nitridation of the *m*-plane sapphire [34]. The mechanical breathing mode is mainly observed in the cavity region. Accordingly, the electric potential inside the AlN pad increases almost monotonically along the direction perpendicular to the 1D nanobeam. Thus, microwave excitation can be coupled with the mechanical breathing mode using the electrodes next to the 1D optomechanical crystal.

The mechanical and optical mode volumes, V_{mech} [8,25] and V_{opt}, respectively, are given by

$$V_{\mathrm{mech}} = \frac{\int_V h(\mathbf{r}) d^3\mathbf{r}}{\max(h(\mathbf{r}))}, \tag{2}$$

$$V_{\mathrm{opt}} = \frac{\int_V \epsilon(\mathbf{r})|\mathbf{e}(\mathbf{r})|^2 d^3\mathbf{r}}{\epsilon(\mathbf{r}_{\max})\max(|\mathbf{e}(\mathbf{r})|^2)}, \tag{3}$$

where ϵ, $\mathbf{e}$, and $\mathbf{r}$ are the permittivity, electric field, and spatial coordinates, respectively. The local energy density, h, averaged over a period, $2\pi/\omega_m$, is given as the sum of the stored strain and kinetic energy densities:

$$h = \frac{1}{4}[Re(\sigma : \bar{T}) + \rho\omega_m{}^2|\mathbf{u}|^2] \tag{4}$$

where σ, T, ρ, and $\mathbf{u}$ are stress, strain, density, and mechanical displacement, respectively. The overbar indicates a complex conjugate.

Surprisingly, the rounded concentrators mediated ultrasmall mode volumes of $V_{\mathrm{mech}} = 1.5 \times 10^{-4}(\Lambda_p)^3, 5.1 \times 10^{-4}(\Lambda_s)^3$, and $V_{\mathrm{opt}} = 0.2(\lambda/n)^3$, where n and λ are refractive index and the wavelength, respectively. The longitudinal and shear wavelengths of the mechanical modes are given as $\Lambda_p = 2\pi\sqrt{E(1-\nu)/[\rho(1+\nu)(1-2\nu)]}/\omega_m$ and $\Lambda_s = 2\pi\sqrt{E/[2\rho(1+\nu)]}/\omega_m$, respectively. Here, E and ν denote the Young's modulus and Poisson ratio, respectively. Our results suggest that a slight asymmetry of the central cavity holes leads to a dramatic reduction of the mode volume in optomechanical cavities. The mechanical quality factor given by the FEM simulation is in the order of 10^9, where loss is solely due to the perfectly matched layers.

Next, we investigated the effects of the positions of the electrodes and the AlN transducer and the distance

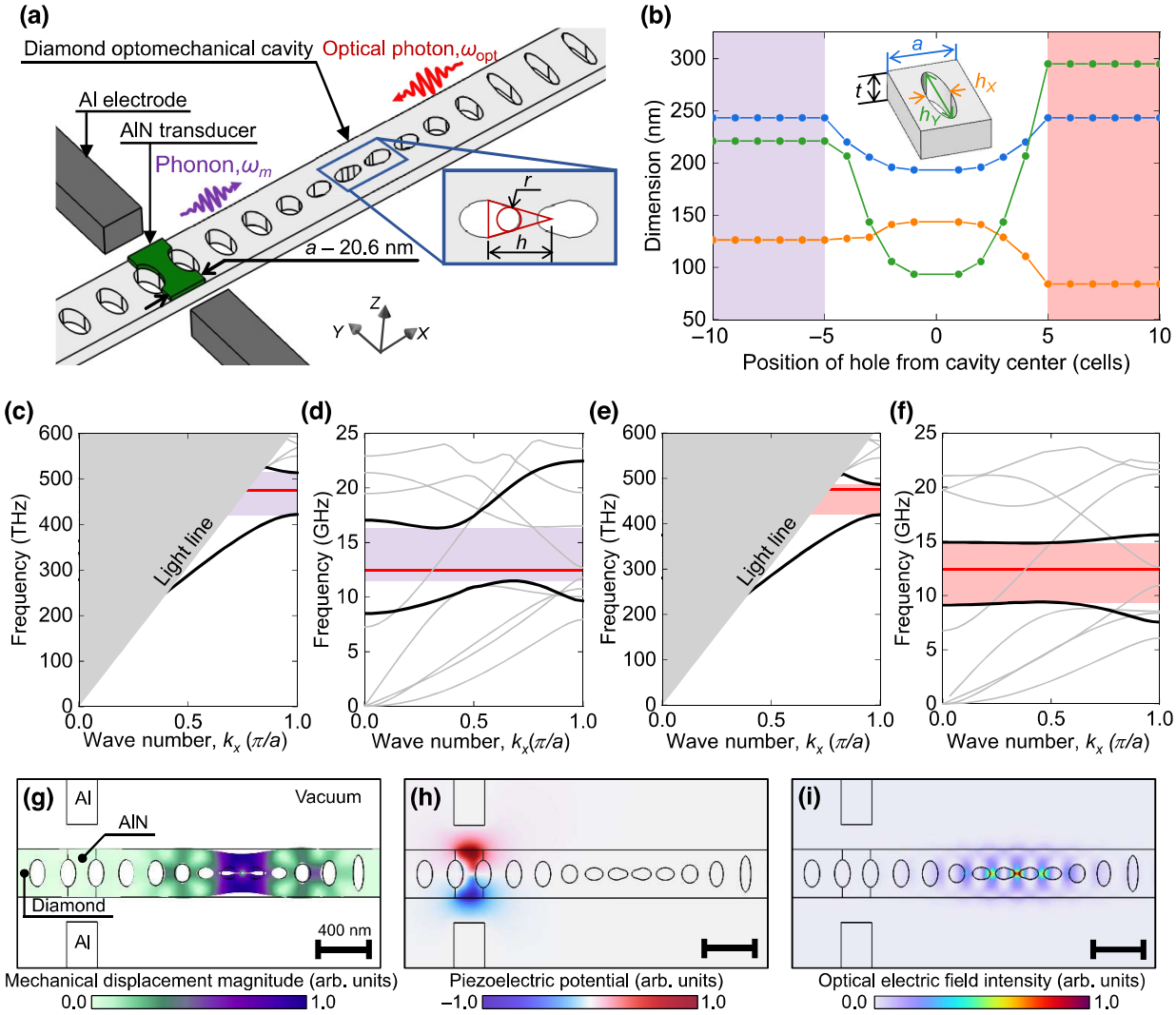

FIG. 2. Design of the microwave-to-optical quantum transduction system using the 1D optomechanical cavity. (a) Overview of the diamond optomechanical cavity with the piezoelectric resonator near the cavity. (b) Dimension of unit cells of the 1D optomechanical cavity. (c),(d) Photonic and phononic band structures of the phononic quasiwaveguide, respectively. (e),(f) Photonic and phononic band structures of the photonic quasiwaveguide, respectively. In (b), purple (red) shaded area means phononic (photonic) quasiwaveguide cells, of which band gaps correspond to the same color in (c)–(f). (g) Displacement distribution of the mechanical resonant mode. (h) Electric potential distribution under mechanical resonance. (i) Electric field distribution of the optical resonant mode.

between concentrator tips (neck), since the optical mode was sensitive to scattering losses. Figures 3(a) and 3(b) show the optical quality factor, Q_{opt}, as a function of the geometries of a piezoelectric resonator. The optical quality factor of the optomechanical cavity is 34 000 without the AlN pad. As shown in Fig. 3(a), when the AlN pad is positioned more than nine holes away from the cavity center, the optical quality factor is not affected by the AlN pad. The FEM simulation errors caused the fluctuation of the optical quality factor, Q_{opt}, around 34 000. Note that the optical quality factor of the current 1D diamond nanobeam crystal cavities experimentally reached 42 000 [35] and 1.76×10^5 [9], which was larger than our designed optical quality factor of about 12 000. Therefore, the deterioration of the optical quality factor would be insignificant considering the use of state-of-the-art fabrication technologies.

For a strong piezoelectric coupling, the AlN pad should be as close as possible to the mechanical cavity for a larger internal electric field. On the other hand, the AlN pad scatters the optical electromagnetic field generated at the photonic cavity. Thus, the position of the AlN pad introduces a trade-off between piezoelectric coupling and the optical quality factor. In this study, considering the photonic bandwidth to cover the mechanically modulated frequency, we placed the AlN pad between two holes with indices of -6 and -7. For $\omega_{opt} \sim 470$ THz, the optical

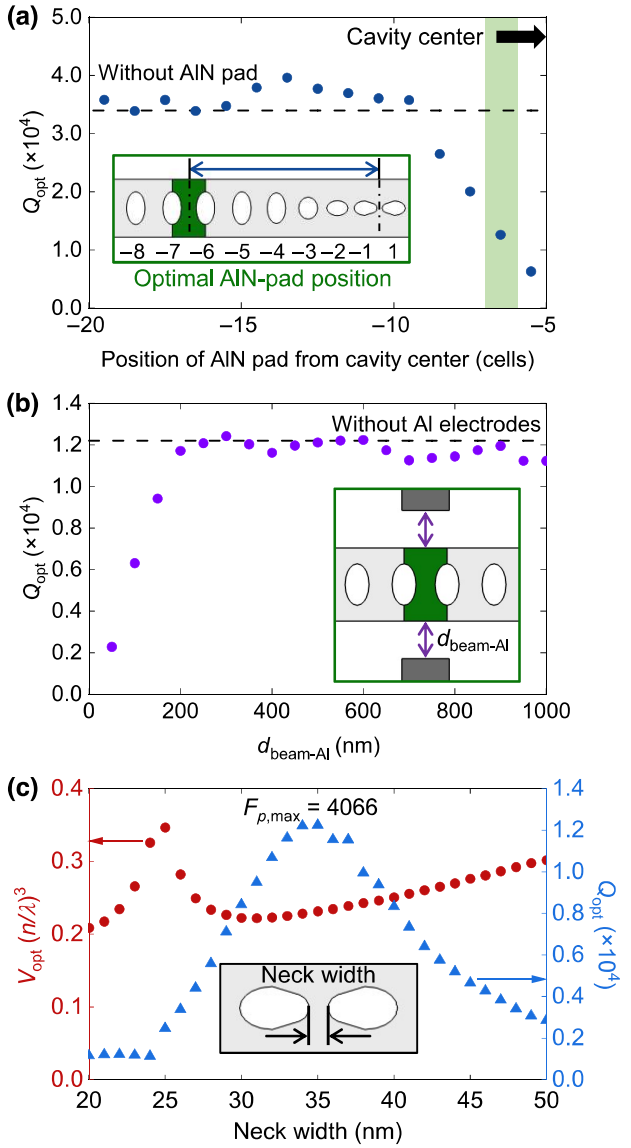

FIG. 3. Optimization of the photonic cavity. (a) Optical quality factor versus position of the AlN pad. Green shaded region is the optimized AlN-pad position. Although the AlN pad should be positioned close to the cavity center for strong piezoelectric coupling, we set the AlN-pad position to keep the optical quality factor over 10 000. (b) Optical quality factor versus distance between the 1D optomechanical crystal beam and the electrode, $d_{beam-Al}$. (c) Optical mode volume and quality factor versus neck width of the concentrators. Insets show schematics of each geometrical parameter.

quality factor, Q_{opt}, of 12 000 has a spectral bandwidth of 39 GHz, which sufficiently covers the microwave modulation of 12.5 GHz. Figure 3(b) shows that the degradation of the optical quality factor due to scattering of the evanescent field becomes negligible when the distance between the 1D beam and the electrode, $d_{beam-Al}$, is larger than 200 nm. In our scheme, since the photonic resonance is at the visible or near-infrared wavelength rather than the communication band (1.5 μm), the width of the 1D nanobeam and $d_{beam-Al}$ can be reduced to enhance piezoelectric coupling.

In the concentrator design, most of the electromagnetic field energy is confined within the neck. Therefore, the neck width between concentrators is an important design parameter for the photonic cavity. Figure 3(c) shows the optical mode volume and quality factor as the neck width is varied. Changing the neck width by a few nanometers leads to a dramatic change in the optical quality factor. On the other hand, the optical mode volume is maintained in the order of $0.2 - 0.3(\lambda/n)^3$. The ultrasmall mode-volume photonic cavity is able to incorporate an extraordinarily large cooperativity with a deep subwavelength structure inside the 1D nanobeam cavity [28–30]. In our design, the maximum Purcell factor was 4066 at a neck width of 35 nm. In practice, the cooperativity of our system can reach up to 10–100, considering the degradation of 1–2 orders of magnitude affected by fabrication imperfection, atomic properties, and orientation [15]. The optical resonant frequency is affected by the dimension of the defects, where the energy of the electromagnetic wave is confined. Thus, the neck width changes the optical resonant frequency. As the optical resonant frequency is set at the band edge [Fig. 1(e)] for implementation of the quasiwaveguide, the neck width has a nontrivial impact on energy leakage to the photonic waveguide, leading to variation of the mode volume appearing at a neck width of about 25 nm.

C. Performances of quantum interfaces

In our previous study [21], we predicted that a significant optical photon-generation rate could enable applications such as remote entanglement generation between superconducting qubits. In our scheme, the two quantum interfaces of the piezoelectric coupling and mechanical-mode–color-center interaction affect the microwave-to-optical conversion efficiency. The piezoelectric coupling rate can be calculated by the overlap integral between an electric field and an electric displacement field [24,36,37]:

$$g_{MW-m} = \frac{1}{2\hbar}\int_V (T^*(\mathbf{r})D^T\mathbf{e}(\mathbf{r}) + \mathbf{e}^*(\mathbf{r})DT(\mathbf{r}))d^3\mathbf{r}, \quad (5)$$

where D indicates the piezoelectric coupling tensor. Figure 4 shows the microwave photon-phonon coupling in the cavity system. The electric field applied from the side of the 1D beam [Fig. 4(a)] leads to excitation of the mechanical breathing mode [Fig. 4(b)]. Note that the microwave-excited vibrational mode is consistent with the mechanical resonant mode in Fig. 1(g). Using Eq. (5), we calculated $g_{MW-m}/(2\pi) = 0.3$ MHz, which was only an order of magnitude smaller than the case of direct electrical excitation near the mechanical cavity reported in Ref. [38].

The N-V^- center has a large mechanical susceptibility of $\chi \approx -0.85$ PHz/strain [39] to the strain tensor component

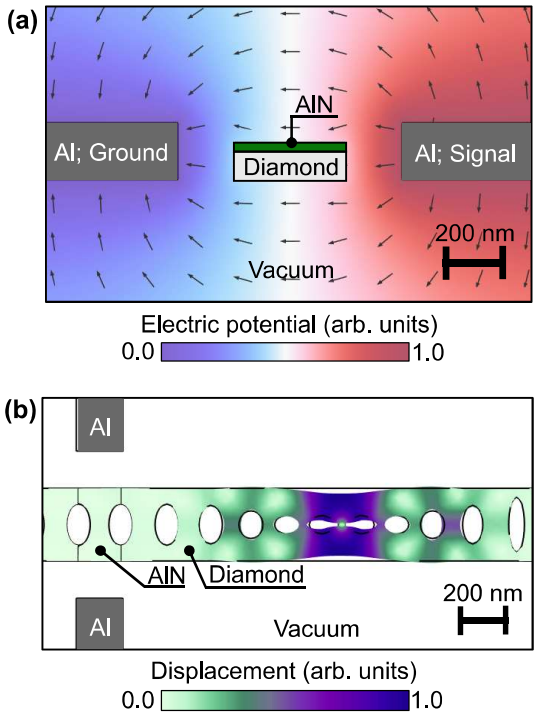

FIG. 4. Microwave photon-to-phonon conversion via piezoelectric coupling. (a) Electric potential profile around the 1D optomechanical crystal under application of the microwave electric field. (b) Resonant mechanical mode of the 1D optomechanical crystal under the microwave electrical field with $\omega_{\mathrm{MW}} \sim$ 12.5 GHz.

of $t_{xx}(\mathbf{r}) - t_{yy}(\mathbf{r})$. The coupling rate between the mechanical mode and the color-center electron is then given by [23,25]

$$g_{m\text{-}e}(\mathbf{r}) = \chi \frac{(t_{xx}(\mathbf{r}) - t_{yy}(\mathbf{r}))}{\max(|\mathbf{u}(\mathbf{r})|)} x_{\mathrm{ZPF}}. \tag{6}$$

The cavity zero-point fluctuation, x_{ZPF}, is given by [23,40,41]

$$x_{\mathrm{ZPF}} = \sqrt{\frac{\hbar}{2m_{\mathrm{eff}}\omega_m}}, \tag{7}$$

where the effective mass of the resonator is

$$m_{\mathrm{eff}} = \frac{\int_V \mathbf{u}^*(\mathbf{r})\rho(\mathbf{r})\mathbf{u}(\mathbf{r})d^3\mathbf{r}}{\max(|\mathbf{u}(\mathbf{r})|^2)}. \tag{8}$$

Considering the use of a diamond (111) slab, we define the high-symmetry axis of the N-V^- center (111) as being along the z axis of the diamond crystal. Accordingly, the x and y axes are along $(\bar{1}\bar{1}2)$ and $(\bar{1}10)$ directions, respectively.

Figure 5 shows the FEM simulation results of the coupling rate between the mechanical mode and the color center, $g_{m\text{-}e}$, in the mechanical cavity. Raniwala *et al.* [23] showed that the Euler angle between the laboratory coordinate system (X,Y,Z) and the crystal coordinate system (x,y,z) had a significant effect on $g_{m\text{-}e}$ due to the anisotropy of the 1D beam. Therefore, we also investigated the effect of the in-plane rotation of the (111) slab as a function of the Euler angle, ϕ, as shown in Fig. 5(a). The rotation of the strain tensor is given by

$$T(x,y,z) = RT(X,Y,Z)R^{-1}, \tag{9}$$

where the rotation matrix, R, is

$$R = \begin{pmatrix} \cos\phi & -\sin\phi & 0 \\ \sin\phi & \cos\phi & 0 \\ 0 & 0 & 1 \end{pmatrix}. \tag{10}$$

In Figs. 5(b) and 5(c), the spatial distribution of $g_{m\text{-}e}$ shows fourfold symmetry, which originates from the diamond cubic crystal. In particular, the strain-tensor component, $t_{xx}(\mathbf{r}) - t_{yy}(\mathbf{r})$, is maximized when $\phi = 0, 90^\circ$ under the resonant mechanical vibration shown in Fig. 2(g). We calculated the maximum to be $g_{m\text{-}e}/(2\pi) = 16.4$ MHz. Figure 5(d) shows that the minimum $g_{m\text{-}e}$ along the concentrator from tip to tip was 45% of the maximum value. Therefore, a high mechanical-mode–color-center coupling rate, $g_{m\text{-}e}/(2\pi)$, on the order of 10 MHz can be obtained as long as the color center can be placed with a spatial accuracy of 20 nm. Note that the maximum optical mode intensity is homogeneous along the neck [Fig. 2(i)], thereby mediating the resonant emission of a photon along the neck, regardless of the position of the color center.

D. Microwave-to-optical conversion efficiency

We estimated the microwave-to-optical conversion efficiency by solving the time evolution of the density matrix, ρ, of the quantum interfaces using a quantum toolbox in PYTHON, QuTiP [42,43]. To investigate the coherent microwave-to-optical conversion efficiency, we set the initial state of the microwave as a weak coherent state, which was approximated as $\exp(-(|\alpha|^2/2))(|0\rangle + \alpha|1\rangle)$. Details of the analytical model are described in Ref. [21]. Here, we simply present the final forms of the equations. Assuming that the microwave and phonon frequencies are nearly equal to the optical detuning frequency, we can model the Hamiltonian of quantum interfaces for microwave-to-optical conversion [21,44]:

$$H_{\mathrm{QI,N\text{-}}V^-} = \hbar\omega_{\mathrm{MW}} a^\dagger_{\mathrm{MW}} a_{\mathrm{MW}} + \hbar\omega_m b^\dagger_m b_m + \hbar\Delta_e \sigma^+_e \sigma_e + \hbar\Delta_{\mathrm{opt}} c^\dagger_{\mathrm{opt}} c_{\mathrm{opt}} + \hbar g_{\mathrm{MW}\text{-}m}(a^\dagger_{\mathrm{MW}} b_m$$

$$+ a_{\mathrm{MW}} b_m^\dagger) + \hbar \frac{\Omega_{\mathrm{Rabi}} g_{m\text{-}e}}{2\omega_m} [(b_m^\dagger - b_m)\sigma_e^+ + (b_m - b_m^\dagger)\sigma_e] + \hbar g_{e\text{-opt}} \left\{ \left[1 + \frac{g_{m\text{-}e}}{\omega_m}(b_m^\dagger - b_m) \right] \sigma_e^+ c_{\mathrm{opt}} + \left[1 + \frac{g_{m\text{-}e}}{\omega_m}(b_m - b_m^\dagger) \right] \sigma_e c_{\mathrm{opt}}^\dagger \right\}, \quad (11)$$

where ω_{MW}, $\Delta_{\mathrm{opt}} = \omega_{\mathrm{opt}} - \omega_d$, and Ω_{Rabi} are the frequency of the microwave photon, optical detuning frequency, and optical Rabi frequency, respectively. $a_{\mathrm{MW}}^\dagger$ (a_{MW}), $b_m^\dagger$ (b_m), and $c_{\mathrm{opt}}^\dagger$(c_{opt}) are the creation (annihilation) operators of the microwave photon in the piezoelectric resonator, phonon in the optomechanical cavity, and photon in the optomechanical cavity, respectively. $\sigma_e^+(\sigma_e)$ is the electron raising (lowering) operator between the ground state and the optically excited state. The master equation in Lindblad form is given by

$$\frac{d\rho}{dt} = \frac{1}{i\hbar}[H_{\mathrm{QI,N\text{-}V^-}}, \rho] + \sum_j \left[\frac{\gamma_j}{2}(2c_j \rho c_j^\dagger - c_j^\dagger c_j \rho - \rho c_j^\dagger c_j) \right], \quad (12)$$

with $c_j = a_{\mathrm{MW}}, b_m, \sigma_e, c_{\mathrm{opt}}$ for the energetic decay of each excitation and $c_j = \sigma_e^\dagger \sigma_e$ for the dephasing of the electron; $\gamma_j = \gamma_{\mathrm{MW}}, \gamma_m, \gamma_e, \gamma_{\mathrm{tot}}, \gamma_e'$ are the corresponding relaxation rates. In Eq. (12), we take coupling to the external photonic waveguide, γ_{WG}, into account, as $\gamma_{\mathrm{tot}} = \gamma_{\mathrm{WG}} + \gamma_{\mathrm{opt}}$, where γ_{opt} is the internal loss rate, which is considered to be $\omega_{\mathrm{opt}}/Q_{\mathrm{opt}}$. Here, we set $\gamma_{\mathrm{WG}} = \gamma_{\mathrm{opt}}$, considering the critical coupling condition between the photonic cavity and the waveguide [45].

We determined the values of the parameters from the FEM simulation results shown in Figs. 2–5 and those reported in the literature: $\omega_{\mathrm{MW}}/(2\pi) = \omega_m/(2\pi) = \Delta_{\mathrm{opt}}/(2\pi) = 12.5$ GHz, $\Omega_{\mathrm{Rabi}}/(2\pi) = 5$ GHz [21], $g_{\mathrm{MW}\text{-}m}/(2\pi) = 0.3$ MHz (FEM simulation), $g_{m\text{-}e}/(2\pi) = 16.4$ MHz, $g_{e\text{-opt}}/(2\pi) = 1$ GHz [15], $\gamma_{\mathrm{MW}}/(2\pi) = 125$ kHz, $\gamma_m/(2\pi) = 568$ kHz (assuming a microwave photonic quality factor of 10^5 [46,47] and mechanical quality factor of 22 000 [48]), and $\gamma_e/(2\pi) = 10$ MHz. While the FEM simulation gives a significantly large mechanical quality factor of 10^9, the mechanical quality factor in experiments is limited by internal losses, such as phonon-phonon scattering and surface scattering induced by fabrication imperfections. Recently, an experiment using a silicon nanocavity achieved a quality factor of about 10^{10} in the millikelvin range [49]. In this study, we adopted a mechanical quality factor of 22 000, which referred to an experiment using a diamond nanocavity under 4 K [48]. We take into account the pure dephasing of N-V^- as $\gamma_e' = 1/T_2^*$, where T_2^* is the pure dephasing time. We vary T_2^* in our simulation.

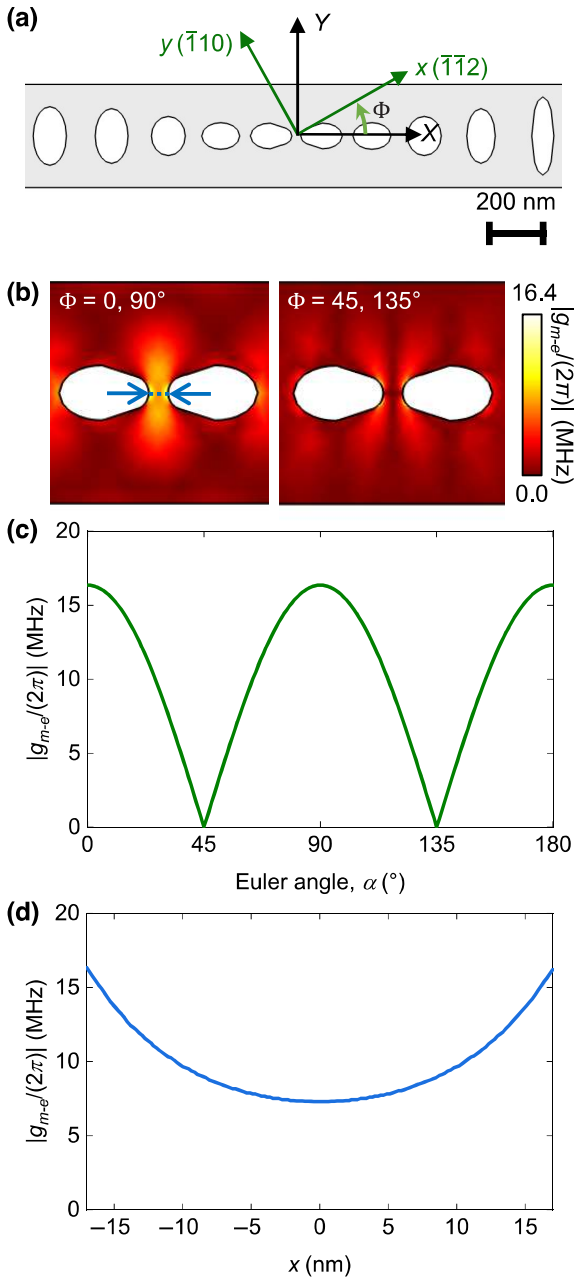

FIG. 5. Coupling rate between the mechanical mode and the color-center electron in the mechanical cavity. (a) Rotation of the diamond crystal orientation with respect to the 1D optomechanical crystal. (b) Spatial distribution of $|g_{m\text{-}e}/(2\pi)|$ for different Euler angles ϕ of 0, 90° (left) and 45, 135° (right). (c) $|g_{m\text{-}e}/(2\pi)|$ at the concentrator tips for different Euler angles ϕ showing the fourfold symmetry. (d) Spatial profile of $|g_{m\text{-}e}/(2\pi)|$ along the neck between the concentrator tips.

Outputs from the photonic cavity to the waveguide are described by the input-output formalism [50–52] written

as

$$d_{\text{out}}(t) = d_{\text{in}}(t) - i\sqrt{\gamma_{\text{WG}}}c_{\text{opt}}(t), \tag{13}$$

where $d_{\text{out}}(t)$ and $d_{\text{in}}(t)$ are input and output operators of the waveguide, respectively. As our scheme can collect photons emitted from an electron of N-V^-, with the discrimination of reflected pumping light, we can neglect the input operator and treat the output as

$$d_{\text{out}}(t) = -i\sqrt{\gamma_{\text{WG}}}c_{\text{opt}}(t). \tag{14}$$

The population of photons in the waveguide is given by the time integral of the expectation value of the number operator, $\left\langle d_{\text{out}}^{\dagger} d_{\text{out}} \right\rangle$. Hence, we define the microwave-to-optical population-conversion efficiency, η_{pop}, as

$$\eta_{\text{pop}} = \frac{\int_0^{t_f} \left\langle d_{\text{out}}^{\dagger} d_{\text{out}} \right\rangle dt}{\left\langle a_{\text{MW}}^{\dagger} a_{\text{MW}} \right\rangle_{t=0}} = \frac{\gamma_{\text{WG}} \int_0^{t_f} \left\langle c_{\text{opt}}^{\dagger} c_{\text{opt}} \right\rangle dt}{\left\langle a_{\text{MW}}^{\dagger} a_{\text{MW}} \right\rangle_{t=0}}, \tag{15}$$

where the measuring time, t_f, is large enough. Similarly, by considering off-diagonal elements of the density matrix as the coherence of the system, the microwave-to-optical coherent conversion efficiency, η_{coh}, is given by

$$\eta_{\text{coh}} = \frac{\int_0^{t_f} |\langle d_{\text{out}} \rangle|^2 dt}{|\langle a_{\text{MW}} \rangle|^2_{t=0}} = \frac{\gamma_{\text{WG}} \int_0^{t_f} \left|\langle c_{\text{opt}} \rangle\right|^2 dt}{|\langle a_{\text{MW}} \rangle|^2_{t=0}}. \tag{16}$$

See the Appendix for the details of their definitions.

First, we simulate an ideal conversion process, i.e., we evaluate the population-conversion efficiency with $T_2^* = \infty$. Figure 6 shows the populations of the quantum interfaces and η_{pop} as a function of the quality parameters of quantum interfaces. In Fig. 6(a), the population of the optical waveguide photon corresponds to a microwave-to-optical conversion efficiency of about 15%. A strong electro-optical coupling, $g_{e\text{-opt}}/(2\pi)$, expedites the generation of an optical photon, leading to a low population of the orbital excited state of N-V^-. Furthermore, since N-V^- has a large strain susceptibility, the population of the waveguide photon is significantly increased by a large mechanical-mode–color-center electron-coupling rate, $g_{m\text{-}e}$, at the mechanical cavity with an ultrasmall mode volume. However, improving $g_{m\text{-}e}$ is limited by the fabrication resolution and the trade-off between the piezoelectric coupling rate, $g_{\text{MW-}m}$, and the optical quality factor, Q_{opt}, as shown in Fig. 3. Accordingly, the enhancement of the microwave-to-optical conversion efficiency relies on the mechanical quality factor, Q_m, and the microwave quality factor, Q_{MW}. Figure 6(b) shows the effect of the mechanical quality factor and the microwave quality factor on η_{pop}. High conversion efficiency, in the range of 15–35%, can be obtained with a moderate improvement in Q_m and Q_{MW}

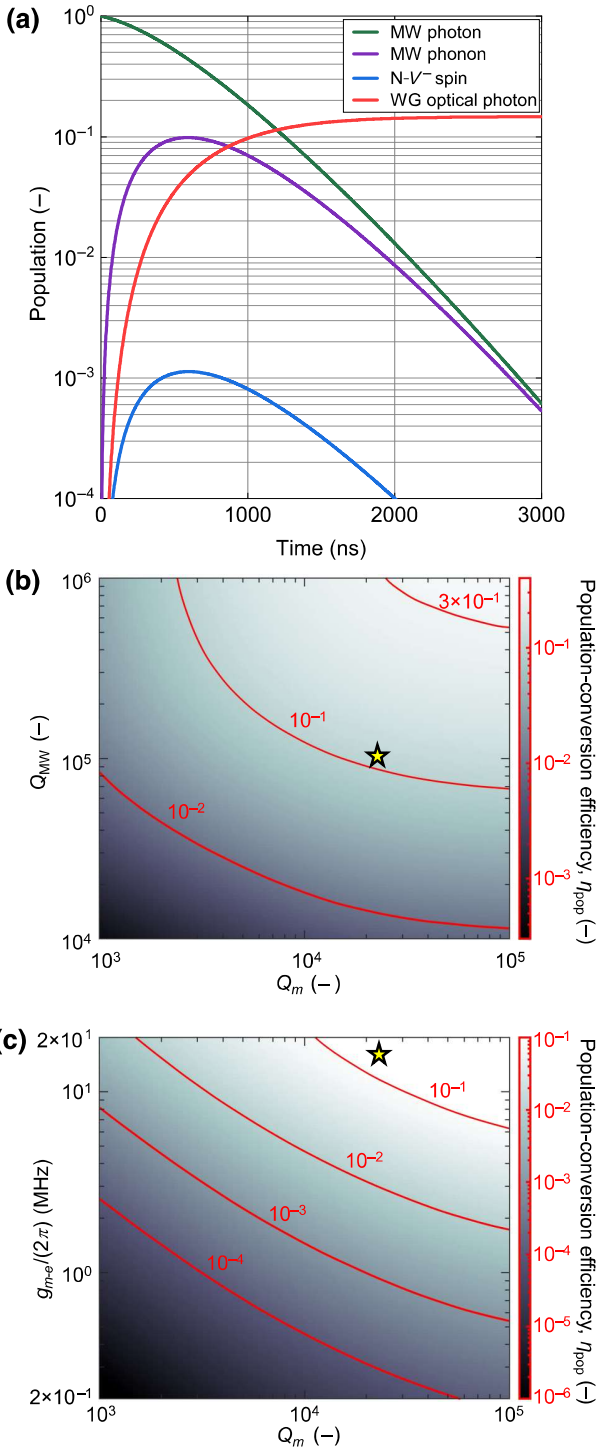

FIG. 6. Population of quanta. (a) Time evolution of the population inside the quantum interface, considering parameters obtained from FEM simulations and state-of-the-art technologies. (b) Population-conversion efficiency, η_{pop}, as a function of the microwave cavity quality factor, Q_{MW}, and mechanical cavity quality factor, Q_m. (c) η_{pop} as a function of the mechanical-mode–color-center electron-coupling rate, $g_{m\text{-}e}$, and Q_m. Star denotes the conditions used in (a): $(Q_{\text{MW}}, g_{m\text{-}e}/(2\pi), Q_m) = (10^5, 16.4\ \text{MHz}, 2.2 \times 10^4)$.

from the condition used in Fig. 6(a), which is indicated by a star.

Nanofabrication of diamond inevitably introduces spectral diffusion of color centers due to defect charges and static strain [53]. Meesala *et al.* [54] showed that the strain susceptibility of a silicon-vacancy center decreased with the presence of static strain, thereby decreasing $g_{m\text{-}e}$ given by Eq. (6). Figure 6(c) indicates η_{pop} as a function of $g_{m\text{-}e}$ and Q_m to investigate the effect of rough side walls introduced by nanofabrication processes. As Q_m over 10^4 has already been demonstrated in the literature [48], achieving $g_{m\text{-}e}/(2\pi)$ larger than 10 MHz is an important challenge for a high population-conversion efficiency, $\eta_{\text{pop}} > 10\%$. Meanwhile, a recent investigation [53] successfully reduced surface damage on diamond nanopillars, showing the long-term linewidth stability of the excited state of the N-V center to be as low as 150 MHz. Therefore, we expect that advances in fabrication technologies will lead to the efficient realization of our scheme in the near future.

Figure 7 shows η_{pop} and η_{coh} as a function of T_2^*, with an amplitude of the weak coherent initial state of $\alpha = 0.1$. With increasing values of T_2^*, η_{coh} asymptotically increased to η_{pop}, and exceeded 10% for T_2^* larger than 10 ns. Experimentally reported values of T_2^* for N-V^- are in the range of 10–80 ns [55]. Thus, coupling between the N-V^- center and the photonic cavity, $g_{e\text{-opt}}/(2\pi)$, is 1–2 orders of magnitude larger than the reported pure dephasing rate, γ_e', implying that our scheme facilitates the coherent microwave-to-optical conversion. We have also checked that these results are independent of α as long as $|\alpha|^2 \ll 1$, which is a natural consequence of the linear response.

Table I summarizes current demonstrations of microwave-to-optical transduction using a piezo-optomechanical transducer along with design values for this study. It is worth noting that direct comparison is difficult because a low microwave-to-mechanical efficiency limits the total conversion efficiency for several reports in the literature

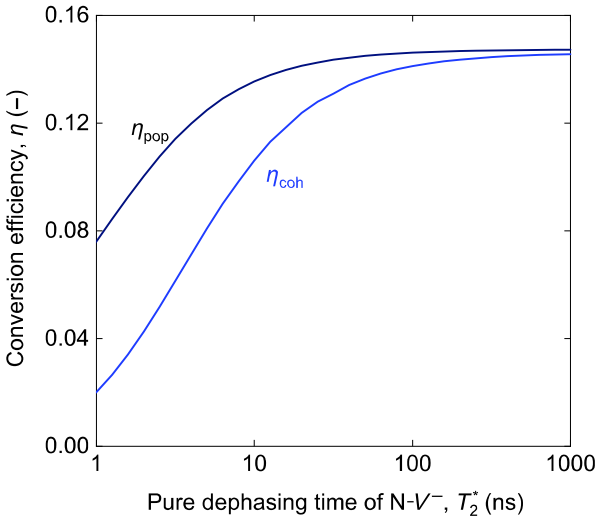

FIG. 7. Microwave-to-optical population and coherent conversion efficiencies as a function of pure dephasing time of N-V^-. Microwave initial state was set as $|0\rangle + \alpha|1\rangle$ with $\alpha = 0.1$.

[2,6,59]. Overall, the performances of the microwave-to-optical quantum interfaces have advanced for various platforms incorporating strong microwave-to-mechanical and optomechanical couplings. Our study intimates that diamond can be a good candidate platform with atomic defects strongly bridging mechanical and optical frequencies. In addition, since our spin-memory-based scheme reduces the optical pump power [21], the mechanical quality factor may be further increased from the result shown in Ref. [48] by decreasing localized phonon-phonon scattering events in nanostructures. Also, a microwave resonator with an internal impedance converter realized a high quality factor over 10^5, paving the way for future progress of fast and active control of superconducting qubits [46]. Therefore, the implementation of our design will lead to

TABLE I. Comparison of piezo-optomechanical transducers for MW-to-optical conversion.

Refs.	Platform	$\omega_{\text{MW}}/(2\pi)$(GHz)	$\omega_{\text{opt}}/(2\pi)$(THz)	$g_{\text{OM}}/(2\pi)$(Hz)[a]	$g_{m\text{-}e}/(2\pi)$(Hz)	η_{pop}
[56]	AlN	3.8	197	1.1×10^5	–	9×10^{-8}
[6]	GaAs	2.7	194	1.3×10^6	–	5.5×10^{-12}
[57]	LN[b]	1.85	195	8×10^4	–	1.1×10^{-5}
[58]	AlN	10	200	1.9×10^4	–	7.3×10^{-4}
[1]	AlN on Si	5.2	194	7×10^5	–	8.8×10^{-6}
[2]	GaP[c]	3.2	193	2.9×10^5	–	1.4×10^{-11}
[59]	GaP	2.8	193	7×10^5	–	6.8×10^{-8}
[60]	LN on Si	3.6	194	4.1×10^5	–	2.5×10^{-2}
This work	Diamond	12.5	470	–	1.6×10^7	1.5×10^{-1}

[a]Optomechanical coupling rate.
[b]Lithium niobate.
[c]Gallium phosphide.

the realization of an unprecedentedly high microwave-to-optical quantum converter, combined with state-of-the-art technologies of nanofabrication and microwave-resonator design.

III. CONCLUSION

We proposed the practical design of quantum interfaces using the photonic cavity at the color-center emission for quantum transduction between microwave and optical photons via diamond spin memories. The pair of noncontact electrodes with the 1D optomechanical crystal cavity could generate a phonon by piezoelectric coupling in the AlN thin-film pad to achieve a reasonable piezoelectric coupling rate of 0.3 MHz. By adopting an ultrasmall mode-volume cavity with rounded concentrators, we calculated the coupling rate, $g_{m\text{-}e}/(2\pi) = 16.4$ MHz, which was 1–2 orders of magnitude larger than typical values, subsequently accelerating emission to the photonic waveguide with the system's population-conversion efficiency being about 15%. Our results imply that an atomic defect coupled to the photonic cavity serves as a coherent quantum transducer, which we predict to have a coherent conversion efficiency of over 10%. We can also consider an alternative color center with a large strain susceptivity, such as the ground state of Si-V^- [61,62]. While our scheme generates noncommunication-band photons, the on-chip nonlinear photonic platform using silicon carbide [63,64] can be effectively used to convert optical frequencies to extend the distance range of the quantum network. Since our system can provide solutions to practical problems, such as conversion efficiency and thermal noise suppression, we expect that the experimental demonstration will open an alternative pathway for the realization of million-node quantum repeaters.

All data are available from the corresponding authors upon reasonable request. The COMSOL simulation file (Figs. 2–5) and Python script (Figs. 6 and 7) are available from a public repository [65].

ACKNOWLEDGMENTS

The authors appreciate M. Yamamoto and Y. Sekiguchi for insightful discussions. This work was supported by a Moonshot R&D grant from the Japan Science and Technology Agency (Grant No. JPMJMS2062) and by a Japan Society for the Promotion of Science Grant-in-Aid for Scientific Research (Grant No. 21H04635).

APPENDIX: DEFINITIONS OF CONVERSION EFFICIENCIES

Here, we address the definitions of η_{pop} and η_{coh} in detail. In a general system, we consider a process where an excitation of one degree of freedom (DOF), denoted by A, is transmitted to other DOFs, B_k, in time t_f. Our aim is to obtain the time evolution of a single-photon input, $|1\rangle_A\,|E\rangle$, where $|E\rangle$ is the initial environment state. The process is represented as

$$|1\rangle_A|E\rangle \to \sum_k C_k(t_f)|1\rangle_{B_k}|E\rangle + \sum_k D_k(t_f)|1\rangle_{B_k}|E'_k\rangle + \sum_F D'_F(t_f)|0\rangle|F\rangle, \tag{A1}$$

where $|E'_k\rangle$ is another state that has the same energy as $|E\rangle$, and $|F\rangle$ is a state with a single excitation added. The second term on the right-hand side of Eq. (A1) represents the coherent transmission of the excitation, while the third term expresses the incoherent transmission. The last term denotes losses of excitation to the environment.

Assuming that we can detect all the excitations of B_k, we can define the efficiency of the total transmission of the population as

$$\eta_{\text{pop}} = \sum_k |C_k(t_f)|^2 + \sum_k |D_k(t_f)|^2, \tag{A2}$$

and the efficiency of the coherent emission as

$$\eta_{\text{coh}} = \sum_k |C_k(t_f)|^2. \tag{A3}$$

For numerically calculating the conversion efficiencies, we can set the initial state as $\alpha|0\rangle + \beta|1\rangle_A$ with $\alpha^2 + \beta^2 = 1$. In terms of correlation functions, we can rewrite Eqs. (A2) and (A3) in the following form:

$$\eta_{\text{pop}} = \frac{\sum_k \left\langle b_k^\dagger b_k \right\rangle_{t=t_f}}{\langle a^\dagger a\rangle_{t=0}}, \quad \eta_{\text{coh}} = \frac{\sum_k |\langle b_k\rangle|^2{}_{t=t_f}}{|\langle a\rangle|^2{}_{t=0}}, \tag{A4}$$

where a and b_k are the annihilation operators for A and B_k, respectively.

For the model we analyze here, the output DOFs correspond to the electric field excited on each spatial point of the waveguide. That is, $b_k \to d_r$ with r denoting the position on the waveguide. Our device is connected to the waveguide at $r = 0$. Experimentally, we can collect all the excitations since they propagate to the detector in order. Note that the coefficients $C_r(t_f)$ and $D_r(t_f)$ are only nonzero when $r < t_f$ holds; the phase velocity is normalized to unity. This is due to the linear propagation of the electric field:

$$d_r(t) = d_{\text{out}}(t - r), \tag{A5}$$

and an assumption that the waveguide's initial state is the ground state. By using the above replacements in Eq. (A4) and noting that $\sum_k \ldots$ corresponds to $\int_0^{t_f} dr \ldots$, which

is equivalent to $\int_0^{t_f} dt \ldots$, we obtain the expression we present in Eqs. (15) and (16).

[1] M. Mirhosseini, A. Sipahigil, M. Kalaee, and O. Painter, Superconducting qubit to optical photon transduction, Nature **588**, 7839 (2020).

[2] S. Hönl, Y. Popoff, D. Caimi, A. Beccari, T. J. Kippenberg, and P. Seidler, Microwave-to-optical conversion with a gallium phosphide photonic crystal cavity, Nat. Commun. **13**, 1 (2022).

[3] J. Bochmann, A. Vainsencher, D. D. Awschalom, and A. N. Cleland, Nanomechanical coupling between microwave and optical photons, Nat. Phys. **9**, 11 (2013).

[4] R. W. Andrews, R. W. Peterson, T. P. Purdy, K. Cicak, R. W. Simmonds, C. A. Regal, and K. W. Lehnert, Bidirectional and efficient conversion between microwave and optical light, Nat. Phys. **10**, 4 (2014).

[5] T. Bagci, A. Simonsen, S. Schmid, L. G. Villanueva, E. Zeuthen, J. Appel, J. M. Taylor, A. Sørensen, K. Usami, A. Schliesser, *et al.*, Optical detection of radio waves through a nanomechanical transducer, Nature **507**, 7490 (2014).

[6] M. Forsch, R. Stockill, A. Wallucks, I. Marinković, C. Gärtner, R. A. Norte, F. van Otten, A. Fiore, K. Srinivasan, and S. Gröblacher, Microwave-to-optics conversion using a mechanical oscillator in its quantum ground state, Nat. Phys. **16**, 1 (2020).

[7] H. Ren, M. H. Matheny, G. S. MacCabe, J. Luo, H. Pfeifer, M. Mirhosseini, and O. Painter, Two-Dimensional optomechanical crystal cavity with high quantum cooperativity, Nat. Commun. **11**, 3373 (2020).

[8] M. Eichenfield, J. Chan, R. M. Camacho, K. J. Vahala, and O. Painter, Optomechanical crystals, Nature **462**, 7269 (2009).

[9] M. J. Burek, J. D. Cohen, S. M. Meenehan, N. El-Sawah, C. Chia, T. Ruelle, S. Meesala, J. Rochman, H. A. Atikian, M. Markham, *et al.*, Diamond optomechanical crystals, Optica **3**, 1404 (2016).

[10] K. C. Balram, M. Davanço, J. Y. Lim, J. D. Song, and K. Srinivasan, Moving boundary and photoelastic coupling in GaAs optomechanical resonators, Optica **1**, 414 (2014).

[11] B. Hensen, H. Bernien, A. E. Dréau, A. Reiserer, N. Kalb, M. S. Blok, J. Ruitenberg, R. F. L. Vermeulen, R. N. Schouten, C. Abellán, *et al.*, Loophole-free bell inequality violation using electron spins separated by 1.3 kilometres, Nature **526**, 7575 (2015).

[12] H. Bernien, B. Hensen, W. Pfaff, G. Koolstra, M. S. Blok, L. Robledo, T. H. Taminiau, M. Markham, D. J. Twitchen, L. Childress, *et al.*, Heralded entanglement between solid-state qubits separated by three metres, Nature **497**, 7447 (2013).

[13] M. Pompili, S. L. N. Hermans, S. Baier, H. K. C. Beukers, P. C. Humphreys, R. N. Schouten, R. F. L. Vermeulen, M. J. Tiggelman, L. dos Santos Martins, B. Dirkse, *et al.*, Realization of a multinode quantum network of remote solid-state qubits, Science **372**, 259 (2021).

[14] M. Ruf, N. H. Wan, H. Choi, D. Englund, and R. Hanson, Quantum networks based on color centers in diamond, J. Appl. Phys. **130**, 070901 (2021).

[15] A. Sipahigil, R. E. Evans, D. D. Sukachev, M. J. Burek, J. Borregaard, M. K. Bhaskar, C. T. Nguyen, J. L. Pacheco, H. A. Atikian, C. Meuwly, *et al.*, An integrated diamond nanophotonics platform for quantum-optical networks, Science **354**, 847 (2016).

[16] C. T. Nguyen, D. D. Sukachev, M. K. Bhaskar, B. Machielse, D. S. Levonian, E. N. Knall, P. Stroganov, C. Chia, M. J. Burek, R. Riedinger, *et al.*, An integrated nanophotonic quantum register based on silicon-vacancy spins in diamond, Phys. Rev. B **100**, 165428 (2019).

[17] N. H. Wan, T.-J. Lu, K. C. Chen, M. P. Walsh, M. E. Trusheim, L. De Santis, E. A. Bersin, I. B. Harris, S. L. Mouradian, I. R. Christen, *et al.*, Large-scale integration of artificial atoms in hybrid photonic circuits, Nature **583**, 7815 (2020).

[18] P. K. Shandilya, D. P. Lake, M. J. Mitchell, D. D. Sukachev, and P. E. Barclay, Optomechanical interface between telecom photons and spin quantum memory, Nat. Phys. **17**, 12 (2021).

[19] J. Borregaard, A. S. Sørensen, and P. Lodahl, Quantum networks with deterministic spin–photon interfaces, Adv. Quantum Technol. **2**, 1800091 (2019).

[20] E. Janitz, M. K. Bhaskar, and L. Childress, Cavity quantum electrodynamics with color centers in diamond, Optica **7**, 1232 (2020).

[21] H. Kurokawa, M. Yamamoto, Y. Sekiguchi, and H. Kosaka, Remote entanglement of superconducting qubits via solid-state spin quantum memories, Phys. Rev. Appl. **18**, 064039 (2022).

[22] P. Ovartchaiyapong, K. W. Lee, B. A. Myers, and A. C. B. Jayich, Dynamic strain-mediated coupling of a single diamond spin to a mechanical resonator, Nat. Commun. **5**, 1 (2014).

[23] H. Raniwala, S. Krastanov, M. Eichenfield, and D. Englund, A spin-optomechanical quantum interface enabled by an ultrasmall mechanical and optical mode volume cavity, arXiv:2202.06999.

[24] H. Raniwala, S. Krastanov, L. Hackett, M. Eichenfield, D. R. Englund, and M. E. Trusheim, Spin-phonon-photon strong coupling in a piezomechanical nanocavity, arXiv:2202.11291.

[25] M. K. Schmidt, C. G. Poulton, and M. J. Steel, Acoustic diamond resonators with ultrasmall mode volumes, Phys. Rev. Res. **2**, 033153 (2020).

[26] J. A. Smith, C. Clear, K. C. Balram, D. P. S. McCutcheon, and J. G. Rarity, Nitrogen-vacancy center coupled to an ultrasmall-mode-volume cavity: A high-efficiency source of indistinguishable photons at 200 K, Phys. Rev. Appl. **15**, 034029 (2021).

[27] H. Choi, D. Zhu, Y. Yoon, and D. Englund, Cascaded cavities boost the indistinguishability of imperfect quantum emitters, Phys. Rev. Lett. **122**, 183602 (2019).

[28] H. Choi, M. Heuck, and D. Englund, Self-similar nanocavity design with ultrasmall mode volume for single-photon nonlinearities, Phys. Rev. Lett. **118**, 223605 (2017).

[29] S. Hu and S. M. Weiss, Design of photonic crystal cavities for extreme light concentration, ACS Photonics **3**, 1647 (2016).

[30] S. Hu, M. Khater, R. Salas-Montiel, E. Kratschmer, S. Engelmann, W. M. J. Green, and S. M. Weiss,

Experimental realization of deep-subwavelength confinement in dielectric optical resonators, Sci. Adv. **4**, eaat2355 (2018).

[31] J. Chan, A. H. Safavi-Naeini, J. T. Hill, S. Meenehan, and O. Painter, Optimized optomechanical crystal cavity with acoustic radiation shield, Appl. Phys. Lett. **101**, 081115 (2012).

[32] J. C. Lagarias, J. A. Reeds, M. H. Wright, and P. E. Wright, Convergence properties of the Nelder-Mead simplex method in low dimensions, SIAM. J. Optim. **9**, 112 (1998).

[33] I. Bryan, Z. Bryan, M. Bobea, L. Hussey, R. Kirste, R. Collazo, and Z. Sitar, Homoepitaxial AlN thin films deposited on *M*-plane $(1\bar{1}00)$ AlN substrates by metal organic chemical vapor deposition, J. Appl. Phys. **116**, 133517 (2014).

[34] Z.-C. Ma, K.-A. Chiu, L.-L. Wei, and L. Chang, Formation of *M*-plane AlN on plasma-nitrided *m*-plane sapphire, Jpn. J. Appl. Phys. **58**, SC1033 (2019).

[35] J. V. Cady, O. Michel, K. W. Lee, R. N. Patel, C. J. Sarabalis, A. H. Safavi-Naeini, and A. C. B. Jayich, Diamond optomechanical crystals with embedded nitrogen-vacancy centers, Quantum Sci. Technol. **4**, 024009 (2019).

[36] C.-L. Zou, X. Han, L. Jiang, and H. X. Tang, Cavity piezomechanical strong coupling and frequency conversion on an aluminum nitride chip, Phys. Rev. A **94**, 013812 (2016).

[37] T. Neuman, M. Eichenfield, M. E. Trusheim, L. Hackett, P. Narang, and D. Englund, A phononic interface between a superconducting quantum processor and quantum networked spin memories, Npj Quantum Inf. **7**, 1 (2021).

[38] P. Arrangoiz-Arriola, E. A. Wollack, M. Pechal, J. D. Witmer, J. T. Hill, and A. H. Safavi-Naeini, Coupling a superconducting quantum circuit to a phononic crystal defect cavity, Phys. Rev. X **8**, 031007 (2018).

[39] K. W. Lee, D. Lee, P. Ovartchaiyapong, J. Minguzzi, J. R. Maze, and A. C. Bleszynski Jayich, Strain coupling of a mechanical resonator to a single quantum emitter in diamond, Phys. Rev. Appl. **6**, 034005 (2016).

[40] S. G. Johnson, M. Ibanescu, M. A. Skorobogatiy, O. Weisberg, J. D. Joannopoulos, and Y. Fink, Perturbation theory for Maxwell's equations with shifting material boundaries, Phys. Rev. E **65**, 066611 (2002).

[41] A. H. Safavi-Naeini and O. Painter, in *Cavity Optomechanics*, edited by M. Aspelmeyer, T. J. Kippenberg, F. Marquardt (Springer Berlin Heidelberg, Berlin, Heidelberg, 2014), pp. 195–231.

[42] J. R. Johansson, P. D. Nation, and F. Nori, QuTiP: An open-source PYTHON framework for the dynamics of open quantum systems, Comput. Phys. Commun. **183**, 1760 (2012).

[43] J. R. Johansson, P. D. Nation, and F. Nori, QuTiP 2: A PYTHON framework for the dynamics of open quantum systems, Comput. Phys. Commun. **184**, 1234 (2013).

[44] D. A. Golter, T. Oo, M. Amezcua, I. Lekavicius, K. A. Stewart, and H. Wang, Coupling a surface acoustic wave to an electron spin in diamond via a dark state, Phys. Rev. X **6**, 041060 (2016).

[45] N. J. Lambert, A. Rueda, F. Sedlmeir, and H. G. L. Schwefel, Coherent conversion between microwave and optical photons—an overview of physical implementations, Adv. Quantum Technol. **3**, 1900077 (2020).

[46] S. Mahashabde, E. Otto, D. Montemurro, S. De Graaf, S. Kubatkin, and A. Danilov, Fast tunable high-*Q*-factor superconducting microwave resonators, Phys. Rev. Appl. **14**, 044040 (2020).

[47] N. Samkharadze, A. Bruno, P. Scarlino, G. Zheng, D. P. DiVincenzo, L. DiCarlo, and L. M. K. Vandersypen, High-kinetic-inductance superconducting nanowire resonators for circuit QED in a magnetic field, Phys. Rev. Appl. **5**, 044004 (2016).

[48] G. Joe, C. Chia, M. Chalupnik, B. Pingault, S. Meesala, E. Cornell, D. Assumpcao, B. Machielse, and M. Lončar, in *2021 Conference on Lasers and Electro-Optics (CLEO)* (2021), pp. 1–2.

[49] G. S. MacCabe, H. Ren, J. Luo, J. D. Cohen, H. Zhou, A. Sipahigil, M. Mirhosseini, and O. Painter, Nano-acoustic resonator with ultralong phonon lifetime, Science **370**, 840 (2020).

[50] K. Koshino, T. Shitara, Z. Ao, and K. Semba, Deterministic three-photon down-conversion by a passive ultrastrong cavity-QED system, Phys. Rev. Res. **4**, 013013 (2022).

[51] C. Ciuti and I. Carusotto, Input-output theory of cavities in the ultrastrong coupling regime: The case of time-independent cavity parameters, Phys. Rev. A **74**, 033811 (2006).

[52] C. W. Gardiner and M. J. Collett, Input and output in damped quantum systems: Quantum stochastic differential equations and the master equation, Phys. Rev. A **31**, 3761 (1985).

[53] L. Orphal-Kobin, K. Unterguggenberger, T. Pregnolato, N. Kemf, M. Matalla, R.-S. Unger, I. Ostermay, G. Pieplow, and T. Schröder, Optically coherent nitrogen-vacancy defect centers in diamond nanostructures, Phys. Rev. X **13**, 011042 (2023).

[54] S. Meesala, Y.-I. Sohn, B. Pingault, L. Shao, H. A. Atikian, J. Holzgrafe, M. Gündoğan, C. Stavrakas, A. Sipahigil, C. Chia, *et al.*, Strain engineering of the silicon-vacancy center in diamond, Phys. Rev. B **97**, 205444 (2018).

[55] A. Batalov, C. Zierl, T. Gaebel, P. Neumann, I.-Y. Chan, G. Balasubramanian, P. R. Hemmer, F. Jelezko, and J. Wrachtrup, Temporal coherence of photons emitted by single nitrogen-vacancy defect centers in diamond using optical Rabi-oscillations, Phys. Rev. Lett. **100**, 077401 (2008).

[56] A. Vainsencher, K. J. Satzinger, G. A. Peairs, and A. N. Cleland, Bi-directional conversion between microwave and optical frequencies in a piezoelectric optomechanical device, Appl. Phys. Lett. **109**, 033107 (2016).

[57] W. Jiang, C. J. Sarabalis, Y. D. Dahmani, R. N. Patel, F. M. Mayor, T. P. McKenna, R. Van Laer, and A. H. Safavi-Naeini, Efficient bidirectional piezo-optomechanical transduction between microwave and optical frequency, Nat. Commun. **11**, 1 (2020).

[58] X. Han, W. Fu, C. Zhong, C.-L. Zou, Y. Xu, A. A. Sayem, M. Xu, S. Wang, R. Cheng, L. Jiang, *et al.*, Cavity piezo-mechanics for superconducting-nanophotonic quantum interface, Nat. Commun. **11**, 1 (2020).

[59] R. Stockill, M. Forsch, F. Hijazi, G. Beaudoin, K. Pantzas, I. Sagnes, R. Braive, and S. Gröblacher, Ultra-low-noise microwave to optics conversion in gallium phosphide, Nat. Commun. **13**, 1 (2022).

[60] W. Jiang, F. M. Mayor, S. Malik, R. Van Laer, T. P. McKenna, R. N. Patel, J. D. Witmer, and A. H. Safavi-Naeini, Optically heralded microwave photon addition, Nat. Phys., 1 (2023).

[61] C. Hepp, T. Müller, V. Waselowski, J. N. Becker, B. Pingault, H. Sternschulte, D. Steinmüller-Nethl, A. Gali, J. R. Maze, M. Atatüre, *et al.*, Electronic structure of the silicon vacancy color center in diamond, Phys. Rev. Lett. **112**, 036405 (2014).

[62] S. Maity, L. Shao, S. Bogdanović, S. Meesala, Y.-I. Sohn, N. Sinclair, B. Pingault, M. Chalupnik, C. Chia, L. Zheng, *et al.*, Coherent acoustic control of a single silicon vacancy spin in diamond, Nat. Commun. **11**, 1 (2020).

[63] M. A. Guidry, K. Y. Yang, D. M. Lukin, A. Markosyan, J. Yang, M. M. Fejer, and J. Vučković, Optical parametric oscillation in silicon carbide nanophotonics, Optica **7**, 1139 (2020).

[64] D. M. Lukin, C. Dory, M. A. Guidry, K. Y. Yang, S. D. Mishra, R. Trivedi, M. Radulaski, S. Sun, D. Vercruysse, G. H. Ahn, *et al.*, 4*H*-Silicon-carbide-on-insulator for integrated quantum and nonlinear photonics, Nat. Photonics **14**, 5 (2020).

[65] https://zenodo.org/record/8378972.